



In situ construction of S-scheme AgBr/BiOBr heterojunction with surface oxygen vacancy for boosting photocatalytic CO₂ reduction with H₂O

Zerui Miao^a, Qingli Wang^a, Yanfeng Zhang^{a,*}, Lingpeng Meng^{a,*}, Xuxu Wang^{b,*}

^a National Demonstration Center for Experimental Chemistry Education, Hebei Key Laboratory of Inorganic Nano-materials, College of Chemistry and Materials Science, Hebei Normal University, Shijiazhuang 050024, PR China

^b State Key Laboratory of Photocatalysis on Energy and Environment, Research Institute of Photocatalysis, College of Chemistry, Fuzhou University, Fuzhou 350108, PR China

ARTICLE INFO

Keywords:

AgBr/BiOBr

Oxygen vacancy

S-scheme heterojunction

Photocatalytic CO₂ reduction

ABSTRACT

S-scheme heterojunction has attracted much attention due to its unique structure and interface interaction. Herein, AgBr/BiOBr heterojunction with surface oxygen vacancies (OVs) was in situ synthesized by a facile chemical method. It was found that the evolution rates of photoreduction of CO₂ to CO and CH₄ with 0.33AB are 212.6 and 5.7 μmol g⁻¹ h⁻¹ respectively, which are 9.2 and 5.2 times higher than those of pure BiOBr. It was demonstrated that the S-scheme band structure could improve the utilization of sunlight, increase the reduction power of photogenerated electrons, and enhance the separation and transfer of photogenerated charge carriers. Furthermore, the OVs on the surface of BiOBr for AgBr/BiOBr heterojunction are conducive to the adsorption and activation of CO₂ molecules. The synergetic effect of S-scheme band structure and OVs on photocatalytic reduction of CO₂ was discussed. The work provides a facile method for in situ construction of S-scheme heterojunction with defect for CO₂ photoreduction.

1. Introduction

Photocatalytic conversion of carbon dioxide into fuel and chemical raw materials helps to reduce human dependence on fossil fuels, which is crucial for solving energy shortage and reducing emissions of CO₂ [1–5]. An efficient CO₂ photocatalytic reduction system requires a wide range of light absorption, high charge separation efficiency, strong capacity of redox and CO₂ adsorption [6]. Unfortunately, the photoreduction of extremely stable CO₂ molecules is very difficult and complex due to the high dissociation energy for C=O bond of 750 kJ·mol⁻¹ [7]. Hence, it is still an enormous challenge to devise highly active photocatalytic systems for the reduction of CO₂.

Solar light driven semiconductor photocatalyst has attracted great attention owing to the suitable redox potential, environmental protection, sustainability and high efficiency. Although many semiconductor photocatalysts, including ZnSe/CdSe [8], CuS/g-C₃N₄ [9], ZnO/Au/g-C₃N₄ [10] and BiOBr [11], have been reported for the photoreduction of CO₂ to fuel, most of them still exhibit low conversion efficiency and uncontrollable selectivity. Therefore, it is necessary to develop stable, efficient and green semiconductor photocatalysts [12]. However, single-component semiconductors usually undergo fast

recombination of photogenerated carriers (h⁺/e⁻), leading to limited applications due to low quantum efficiency [13]. To solve this obstacle, researchers have made a lot of efforts to enhance the performance of the catalyst, such as depositing precious metals [14], doping atoms [15] and building heterojunctions [16–19]. Recently, the construction of heterojunctions by coupling semiconductors is considered to be a very feasible strategy for photocatalyst modification. It is worth noting that the construction of S-scheme heterojunction can accelerate the separation and transfer of h⁺/e⁻ and maintain a strong redox ability compared with the traditional type II heterojunction, such as BiOCl/CuBi₂O₄ [20], CeO₂/BiOI [21], CeO₂/PCN [22], etc. Nevertheless, it is still an imperative to construct novel S-scheme heterojunctions with excellent activity for CO₂ photocatalytic reduction through a facile synthesis process.

So far, bismuth-based photocatalysts have received extensive attention in the fields of hydrogen hydrolysis, pollutant photodegradation, and carbon dioxide reduction due to their unique anisotropic structure, good optical and electrical properties [23,24]. In particular, BiOX of the layered ternary oxide (X = Cl, Br and I) has excellent photocatalytic performance. Among them, BiOBr is widely investigated owing to the relatively narrow band gap of 2.7 eV and the proper position of conduction band and valence band. In addition, BiOBr with layered

* Corresponding authors.

E-mail addresses: zhangyanfeng@hebtu.edu.cn (Y. Zhang), menglpl@hebtu.edu.cn (L. Meng), xwang@fzu.edu.cn (X. Wang).

<https://doi.org/10.1016/j.apcatb.2021.120802>

Received 21 July 2021; Received in revised form 22 September 2021; Accepted 2 October 2021

Available online 9 October 2021

0926-3373/© 2021 Elsevier B.V. All rights reserved.

structure is apt to produce OV's due to the weak Bi—O bond [7]. OV's are considered to be the trapping centers of photogenerated electron to promote the separation of charge carriers. Furthermore, OV's exhibit abundant local electrons and neighbouring defected states, which could be conducive to the adsorption and activation of the reactants in the catalytic process [25–27]. Therefore, it is expected to rationally construct the heterojunction by BiOBr with rich OV's as carrier transfer channel to boost the photocatalytic activity.

Silver halide, particularly AgBr, is one of importance light-sensitive materials, which has been widely used in composite photocatalytic system due to excellent electronic properties and photocatalytic performance. However, AgBr is unstable and easily reduced to metal Ag under the illumination [28–30]. Thus, in order to make full use of the photocatalytic activity, the materials are usually loaded on AgBr to inhibit its reduction and improve the stability of AgBr, such as AgBr/WO₃ [31], AgBr/g-C₃N₄ [32], etc. Moreover, it is still a challenge to construct the close contacted interface between BiOBr and the coupling materials due to the difficulty in controlling the crystallinity and morphology, which inhibits the further improvement of activity for BiOBr-based photocatalysts. Generally, heterojunction constructed by AgBr and BiOBr can improve the utilization of sunlight, charge separation efficiency, ability of redox and CO₂ adsorption to boosting the photocatalytic of CO₂ reduction. Especially, the two materials in the heterogeneous share a common element, which is beneficial to build a close contact interface [12,33,34]. Recently, AgBr/BiOBr heterojunction has been constructed for degradation of organic pollutant and bactericidal [35–37]. However, few researches have been done in situ synthesis and photocatalytic reduction of CO₂ for AgBr/BiOBr heterojunction.

Herein, AgBr/BiOBr heterojunctions with different molar ratios were in situ prepared by a facile chemical method under water bath. The effects of molar ratios of AgBr/BiOBr, dosage of H₂O, irradiation time and light intensity on the CO₂ photoreduction efficiency were determined in the absence of photosensitizer and sacrificial agent. It was found that the evolution rate of CO in 0.33AB heterojunction is 212.6 $\mu\text{mol g}^{-1} \text{h}^{-1}$, which is 9.2 times higher than that of single BiOBr. The experimental results and theoretical calculations show that in situ as-prepared AgBr/BiOBr with OV's exhibits an S-scheme band structure, which could improve charge-separation efficiency, redox ability and adsorption and activation of CO₂, therefore boosting the photocatalytic activity of CO₂ reduction.

2. Experimental

2.1. Preparation of samples

All reagents are analytical grade and employed without further purification. 3 mmol of Bi(NO₃)₃·5H₂O was dissolved in 45 mL of ethylene glycol. 0.75, 1, 0.5, 3 and 9 mmol of AgNO₃ and 6 mmol of NaBr were dispersed in 22.5 mL of deionized water, respectively. Bi(NO₃)₃ solution and AgNO₃ solution are mixed with stirring for 30 min, denoted as solution A. Subsequently, NaBr solution was added into solution A with magnetic stirring for 2 h under water bath at 90 °C. The prepared precipitates were cooled to room temperature, collected by filtration, washed several times with deionized water, and dried at 80 °C for 10 h to obtain AgBr/BiOBr powders with different molar ratios. For comparison, pure AgBr and BiOBr were synthesized, as shown in Fig. S1. For convenience, the as-prepared AgBr/BiOBr with different molar ratios (AgBr:BiOBr = 1:4, 1:3, 1:2, 1:1, 3:1) are named as 0.25AB, 0.33AB, 0.5AB, AB and 3AB, respectively.

2.2. Material characterizations

The crystal structure of catalyst was detected on D8 X-ray diffractometer (XRD) employing Cu K α as radiation source. The morphology and energy dispersive X-ray spectrometer (EDX) of catalyst were examined through S-4800 scanning electron microscope (SEM) and field

emission transmission electron microscope (FETEM, JEM-F200). The light intensities of xenon lamp were detected employing an ILT 950 spectroradiometer. X-ray photoelectron spectrometer (XPS) data were recorded on ESCALAB 250 spectrometer. The O-K edge of soft X-ray absorption spectra (XAS) was measured at the 08U1A beam station of the Shanghai Synchrotron Radiation Facility. CO₂ adsorption and the specific surface area detection were performed on Beijing Aode surface area analyzer. The UV–vis diffuse reflectance spectrum (UV–vis DRS) of the catalyst was examined via the Hitachi U-4100 spectrophotometer. Photoluminescence (PL) spectra were obtained on FLS980 with an excitation wavelength of 380 nm. Nanosecond level time-resolved fluorescence (TPRL) decay curve were investigated through a steady-state/transient fluorescence spectrometer (FLS980, Edinburgh Instruments, UK). In-situ Fourier Infrared Spectroscopy (FTIR) (Nicolet 670) spectra was measured in the process of photoreduction of CO₂. Electron spin resonance (ESR) spectra were recorded on MS-5000 electron spin paramagnetic resonance.

2.3. Photocatalytic reduction CO₂

A 300 W Xenon lamp (PLS-SXE 300D, Beijing Perfectlight) is selected as the light source to simulate sunlight. First of all, 10 mg of sample was added into a 200 mL Schlenk bottle sealed with silicone rubber septum. Then the reactor was released the air and filled with CO₂ gas of high purity by mechanical pump for 3 times to ensure the purity of CO₂ in the Schlenk bottle. Subsequently, 5 μL of pure H₂O was injected into the bottle. After 3 h of light reaction, an Agilent GC-7890B gas chromatograph equipped with FID detector, TCD detector and column (TDX-01) was employed to analyze the product.

2.4. Photoelectrochemical measurement

In the electrochemical test, transient photocurrent spectroscopy, electrochemical impedance spectrum (EIS) and Mott-Schottky (MS) curves were obtained by the CHI600E electrochemical workstation of China. The counter electrode and reference electrode were platinum electrode and Ag/AgCl, respectively. First, 10 mg of the sample was put into 7 mL of ethanol and sonicated for 1 h to obtain a uniform suspension. Next, the working electrode is made by spraying suspension liquid on conductive glass (1 \times 2 cm) and dried naturally. The transient photocurrent was detected with 0.5 M Na₂SO₄ solution as electrolyte solution with 300 W Xenon lamp.

2.5. DFT calculations

First-principles calculations based on density functional theory (DFT) were performed employing Vienna Ab initio Simulation Package (VASP) with plane-wave pseudopotential basis [38]. Perdew-Burke-Ernzerhof (PBE) [39] functional in the framework of generalized gradient approximation (GGA) [40] was used to describe the exchange and correlation interaction. Heterojunction models, BiOBr/AgBr and AgBr/BiOBr, were constructed from pristine BiOBr and AgBr crystals. Using 500 eV of plane wave cut-off energy, the heterojunction structures were fully optimized until the residual force on each atom is less than 0.02 eV/Å, ensuring their stable configurations. A vacuum of 15 Å was set between the plates in calculations in order to reduce the interaction between repeated plates. The band structure, density of states, and CO₂ adsorption energy were calculated at DFT level. The work function (Φ) was obtained by subtracting the Fermi level (E_F) from the electrostatic potential of the vacuum level (E_{vac}) ($\Phi = E_{\text{vac}} - E_F$).

The CO₂ adsorption energies on the surface of pure BiOBr and AgBr, as well as two sides of AgBr/BiOBr heterojunction were calculated by the formula (1):

$$E_{\text{ad}} = E_{\text{total}} - E_{\text{slab}} - E_{\text{CO}_2} \quad (1)$$

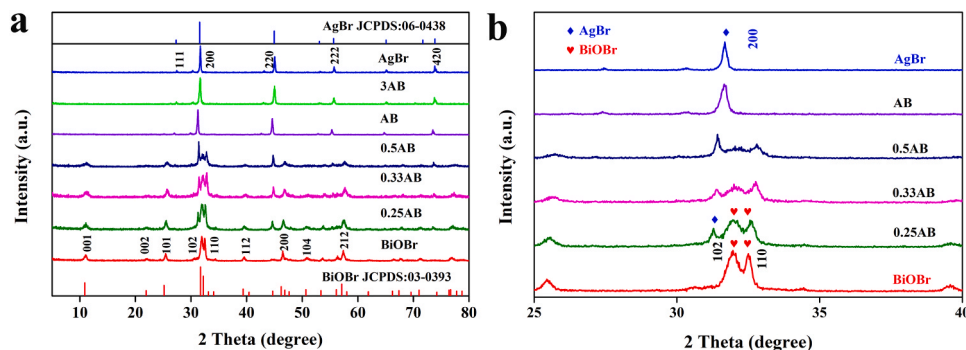


Fig. 1. (a) XRD patterns, and (b) enlarged XRD patterns of pure BiOBr, pure AgBr and AgBr/BiOBr heterojunction.

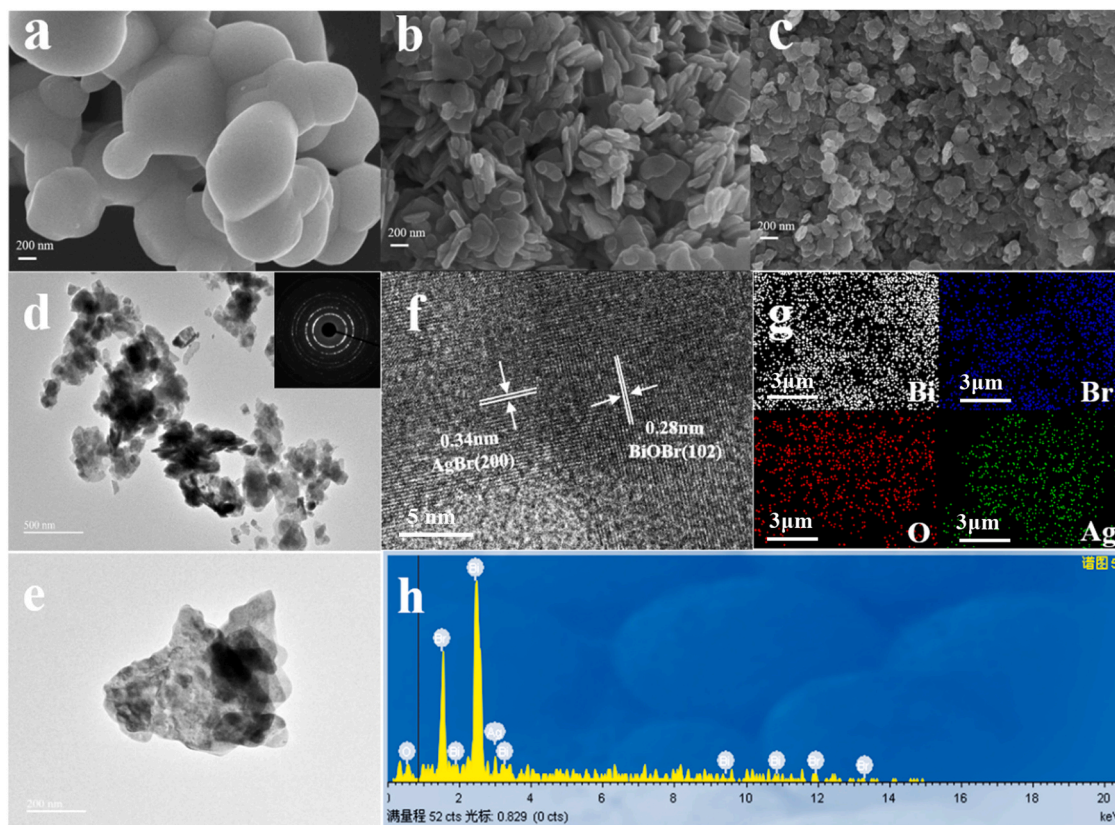


Fig. 2. SEM images of (a) pure AgBr, (b) pure BiOBr and (c) 0.33AB. (d-e) TEM and SAED images (inset) of 0.33AB, (f) HRTEM of 0.33AB, (g) elemental mapping images of 0.33AB, (h) EDX spectrum of 0.33AB.

where E_{total} , E_{slab} , and E_{CO_2} represent the total energies of adsorbed system, pure BiOBr, or AgBr, or heterojunction, and CO_2 molecule.

3. Results and discussion

3.1. Crystal structure and morphology

Fig. 1a shows the XRD patterns of pure BiOBr, pure AgBr and AgBr/BiOBr with various molar ratios. It was found that pure BiOBr, pure AgBr, and AgBr/BiOBr with various molar ratios are clearly identifiable by the characteristic peaks of tetragonal BiOBr (JCPDS No. 03-0393) and face-centered-cubic AgBr (JCPDS No. 06-0438) [41]. The diffraction peaks are sharp, indicating superior crystallinity of these samples. The diffraction peaks of BiOBr gradually decrease with the increase of AgBr, suggesting coexistence of BiOBr and AgBr. Moreover, as the content of AgBr decreases, (110) peak of BiOBr increases and (102) peak

of the BiOBr decreases, indicating that AgBr can affect the growth direction of BiOBr owing to the interface interaction between AgBr and BiOBr (Fig. 1b).

Fig. 2a shows the SEM image of pure AgBr, indicating an uneven block structure. The as-prepared pure BiOBr is composed of irregular nanosheets with the thickness of 20–50 nm (Fig. 2b). Fig. 2c displays the SEM images of 0.33AB, displaying nanosheet structure with thickness of 10–30 nm. The SEM images of the other heterojunctions with different molar ratios are shown in the Fig. S2(a-d). Furthermore, the nanosheets morphology of 0.33AB is verified by TEM (Fig. 2d and e). 0.33AB exhibits the smaller and thinner nanosheets, compared with the pristine BiOBr. It is possible that two kinds of substances for AgBr and BiOBr are generated simultaneously, occupied.

the space and restricted each other's growth in the synthesis process. The microstructure of 0.33AB was observed by HRTEM (Fig. 2f), clearly demonstrating intimate contact interface of the heterojunction and the

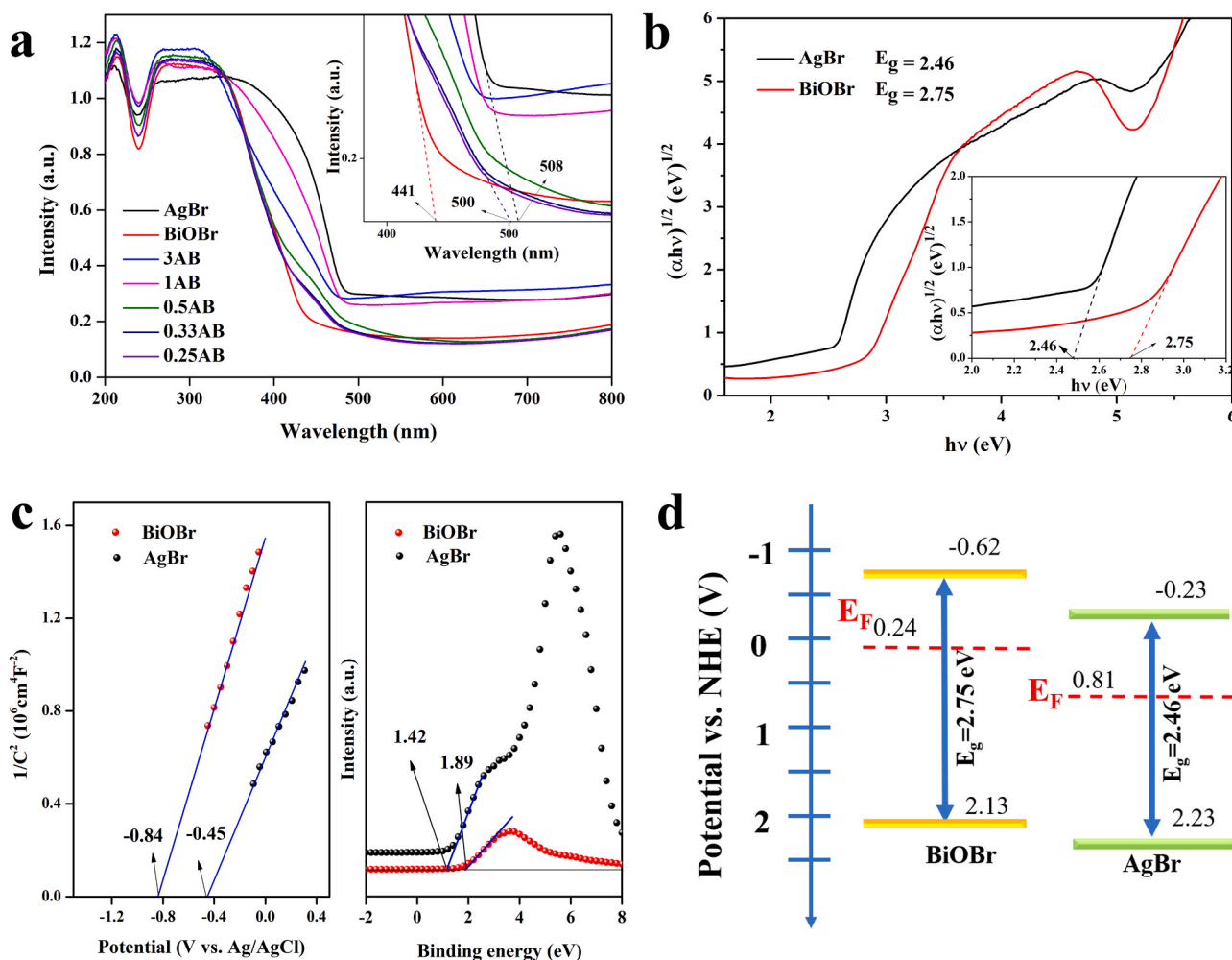


Fig. 3. (a) UV-vis DRS of pure AgBr, pure BiOBr and AgBr/BiOBr with different ratios. (b) Band gap energies, (c) Mott-Schottky curves (left) and VB XPS (right) and (d) band structure of pure AgBr and BiOBr.

lattice spacings of 0.34 and 0.28 nm, which could be attributed to AgBr (2 0 0) plane and BiOBr (1 0 2) plane, respectively [42,43]. The selected area electron diffraction (SAED) of 0.33AB is displayed in Fig. 2d (inset), suggesting its polycrystalline structure. The elements of Bi (white), O (red), Br (blue), and Ag (green) are uniformly distributed in 0.33AB heterojunction (Fig. 2g). Moreover, EDX spectrum of 0.33AB is shown in Fig. 2h. EDX spectra and contents of Bi, Br, O and Ag atoms of others AgBr/BiOBr heterojunctions are shown in Fig. S3, and Table S1, further confirming the element ratios are close to the initial materials.

3.2. Electronic band structure

The UV-vis diffuse reflectance spectra of pure AgBr, pure BiOBr and AgBr/BiOBr heterojunction with different ratios are shown in Fig. 3a. The cut-off absorption edge of pure BiOBr is at 441 nm. The light absorption edge is located near 508 nm for AgBr, which displays better visible light response. 0.33AB exhibits enhancement of light response in the visible light region with coupling of AgBr and BiOBr. The band gap energies of pure BiOBr and AgBr were estimated by the following Eq. (2).

$$A h\nu = A (\alpha h\nu - E_g)^{n/2} \quad (2)$$

where α , $h\nu$, A and E_g represent the absorption coefficient, photon energy, a constant, and band gap respectively [44]. The value of n is 4 owing to the indirect semiconductor characteristics of BiOBr and AgBr. The band gaps of pure BiOBr and AgBr are 2.75 eV and 2.46 eV

respectively, which are basically consistent with the value reported in the literature (Fig. 3b). Furthermore, the flat band potentials of pure BiOBr and AgBr were further measured by Mott-Schottky curves. The positive slope of the Mott-Schottky curves shows that both BiOBr and AgBr are n-type semiconductors (left, Fig. 3c). The flat band (E_{fb}) potentials of pure BiOBr and AgBr are -0.62 and -0.23 V vs. NHE respectively [45]. Subsequently, the CB of BiOBr and AgBr are estimated to be -0.62 V and -0.23 V vs. NHE, respectively, due to the conduction band (CB) potential of n-type semiconductor close to the E_{fb} . The valence band (VB) potential of BiOBr and AgBr can be estimated through E_g and E_{fb} , which are 2.13 and 2.23 V vs. NHE, respectively. The distance from the valence band to the Fermi level can be determined by the VB XPS of pure BiOBr and AgBr (right, Fig. 3c), illustrating that the Fermi levels of pure BiOBr and AgBr are 0.24 and 0.81, respectively. Fig. 3d exhibits the band structure of pure BiOBr and AgBr respectively.

3.3. Photoreduction CO_2 performance

The photocatalytic activities of CO_2 reduction on pure BiOBr, pure AgBr and AgBr/BiOBr with different molar ratios were evaluated with pure H_2O under the irradiation of simulated sunlight for 3 h (Fig. 4a). The three parallel experimental data is shown in the Table S2. It can be observed that the main product of the CO_2 photocatalytic reduction is CO [46,47]. 0.33AB displays the best photocatalytic activity among all of the catalysts with the evolution rate of CO and CH_4 of $212.6 \mu mol g^{-1}$

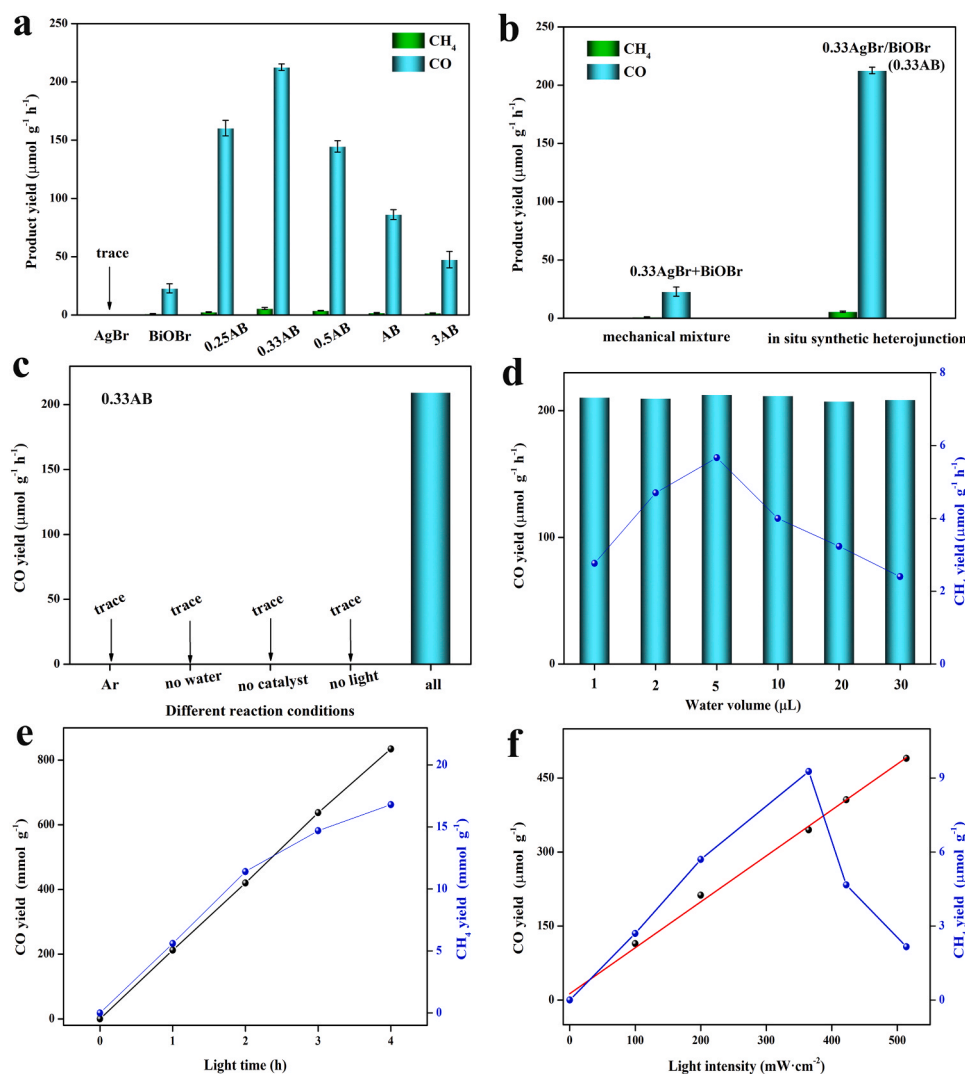


Fig. 4. Yield of CH₄ and CO with (a) various catalysts, and (b) mechanical mixture of AgBr and BiOBr; in situ synthesized 0.33AB. (c) Yield of CO on 0.33AB with different reaction conditions. Change in the (d) H₂O, (e) irradiation time and (f) light intensity effects on yield of CO and CH₄.

h⁻¹ and 5.7 μmol g⁻¹ h⁻¹, which are 9.2 times and 5.2 times higher than that of pristine BiOBr. Among AgBr/BiOBr heterojunctions with different ratios, the photocatalytic activity of 0.33AB is higher than that of others, indicating that there is an optimal amount of AgBr/BiOBr heterojunction. 0.33AB exhibits better photocatalytic activity compared with the previously reported representative photocatalysts (Table S3). Fig. 4b shows the comparison of photocatalytic activity of CO₂ photoreduction with the as-prepared AgBr/BiOBr heterojunction and the mechanical mixture of pure AgBr and pure BiOBr. It is found that the yields of CO and CH₄ with AgBr/BiOBr heterojunction are dramatically higher than those of the mechanical mixture, indicating that the heterojunction structure plays a vital role in the process of CO₂ photoreduction [48]. Fig. 4c presents the effect of different experimental conditions on the photocatalytic activity for CO₂ reduction with 0.33AB. No reduction products are detected in Ar atmosphere without.

CO₂, suggesting that the product of CO is originated from the filled CO₂, and it is found that no reduction products are present in the absence of H₂O, light, and catalyst respectively, indicating that CO₂, H₂O, light and catalyst are indispensable factors in the photoreduction reaction of CO₂. Furthermore, the effect of the amount of H₂O on the reaction products is explored (Fig. 4d). Different amounts of H₂O have no obvious effect on CO₂ photocatalytic reduction to CO. However, the reduction of CH₄ is the largest with 5 μL of H₂O, indicating that the

lower and higher dosage of H₂O are not conducive to the reduction reaction. Fig. 4e displays the evolution rates of CO and CH₄ on 0.33AB with the light irradiation time of 4 h. The evolution rate of CO and CH₄ on 0.33AB increase with the light intensity enhancing (Fig. 4f). It is found that the rate of reduction to CO is first-order reaction, which is a rate-limiting step in the entire reaction ($\text{CO}_2 + 2\text{e}^- + 2\text{H}^+ = \text{CO} + \text{H}_2\text{O}$). However, it is difficult to produce CH₄ because more electrons and protons are needed ($\text{CO}_2 + 8\text{e}^- + 8\text{H}^+ = \text{CH}_4 + 2\text{H}_2\text{O}$) [49]. Thus, the product CO displays higher yield than CH₄ because the reduction to CO and CH₄ could be a pair of parallel reactions.

3.4. XPS and O K-edge XAS

Fig. S4 exhibits the survey XPS spectra of pure BiOBr, pure AgBr and 0.33AB respectively, demonstrating that Bi, Br, O, and Ag elements exist in 0.33AB. Fig. 5 presents the high-resolution spectra of Bi 4f, Ag 3d, O 1s and Br 3d respectively. In Fig. 5a, the four symmetrical characteristic peaks of 158.8 eV, 159.4 eV, 164.3 eV, and 164.7 eV match with Bi 4f_{7/2} and Bi 4f_{5/2} of Bi^{(3-x)+} and Bi³⁺ in pure BiOBr respectively. The four peaks of Bi 4f_{7/2} and Bi 4f_{5/2} in 0.33AB shift to higher binding energy in the dark, suggesting that the charge of Bi³⁺ decreases compared with AgBr/BiOBr heterojunction. However, Bi 4f_{7/2} and Bi 4f_{5/2} in 0.33AB shift to lower binding energy under the light, indicating that the Bi

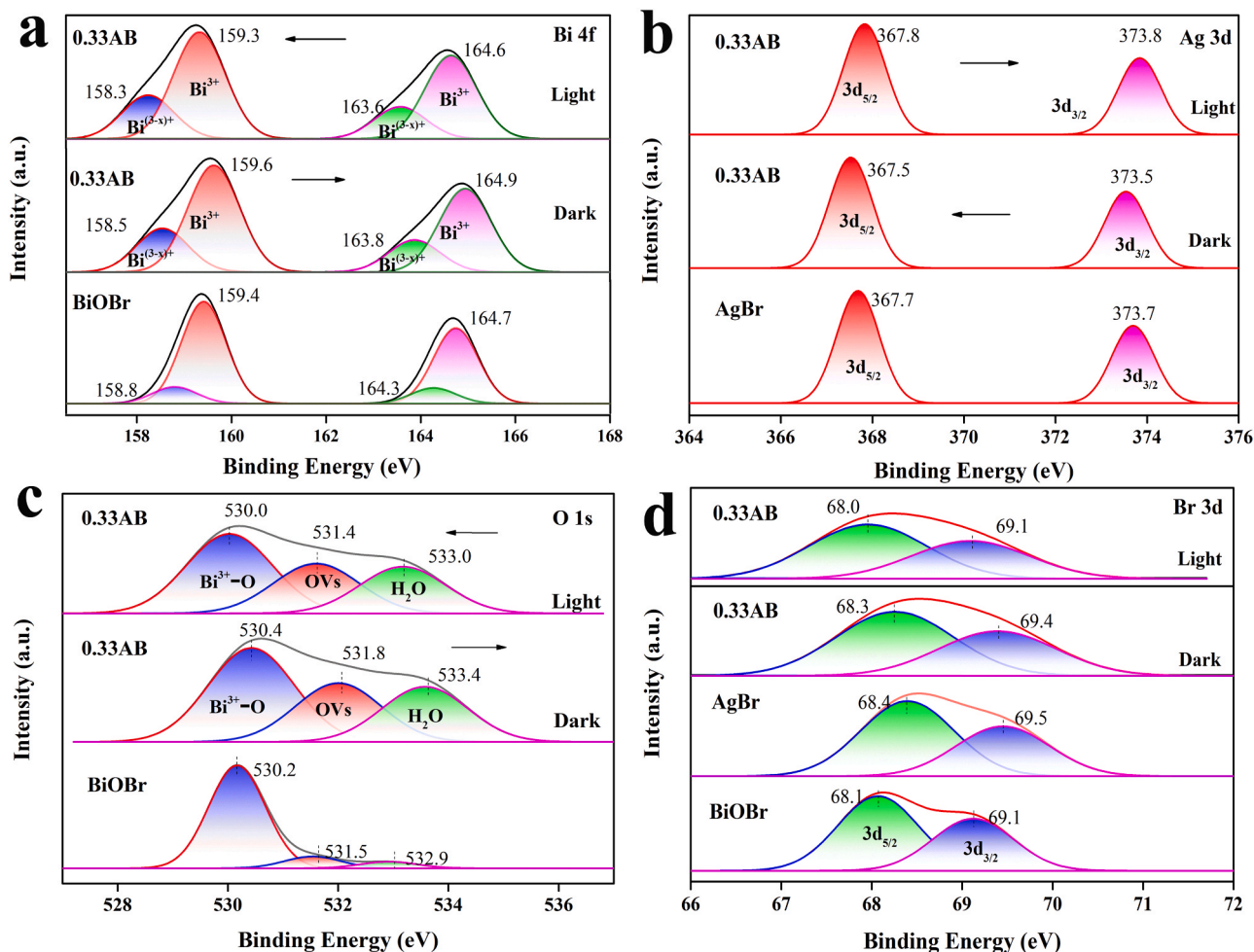


Fig. 5. High-resolution XPS spectra of (a) Bi 4f, (b) Ag 3d, (c) O 1s and (d) Br 3d for pure BiOBr, pure AgBr and 0.33 AgBr/BiOBr in darkness and under illumination.

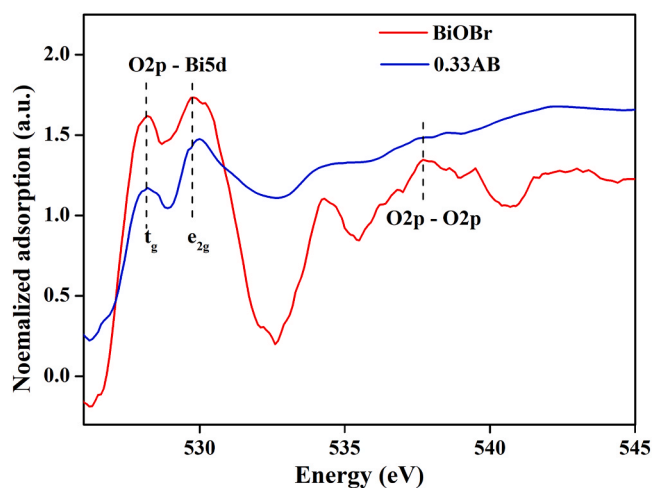


Fig. 6. O K-edge of XAS for pure BiOBr and 0.33AB.

species of BiOBr component in AgBr/BiOBr is electron acceptor under illumination. The characteristic peak of $\text{Bi}^{(3-x)+}$ is obviously enhanced, indicating that more OV are formed in 0.33AB induced by the interfacial interaction of BiOBr and AgBr [50]. In Fig. 5b, it can be found that the two peaks at 367.7 eV and 373.7 eV belong to Ag $3d_{5/2}$ and Ag $3d_{3/2}$, respectively. Whereas the two peaks of Ag 3d for 0.33AB shift to lower binding energy in the dark and higher binding energy in the light

compared with pure AgBr, indicating that the charge transfer from BiOBr to AgBr in the absence of illumination but AgBr to BiOBr under illumination [51]. Furthermore, the XPS spectra of O elements of pure BiOBr can be fitted into three peaks located at 530.2, 531.5 and 532.9 eV, which correspond to Bi-O, OV, and surface hydroxyls, respectively (Fig. 5c) [52]. The peak of lattice oxygen in AgBr/BiOBr shifts to higher energy of 530.4 eV in dark and lower energy of 530.0 eV after illumination in contrast with pure BiOBr. Obviously, the concentration of OV and surface hydroxyls of 0.33AB is much higher than that of pure BiOBr. Fig. 5d shows the Br 3d spectra of pure AgBr, pure BiOBr and 0.33AB respectively, illustrating that the peaks located at 68.3 and 69.4 eV are attributed to Br $3d_{5/2}$ and Br $3d_{3/2}$ of 0.33AB, respectively. The two peaks of Br 3d for 0.33AB shift to higher and lower energy in the dark compared with pure BiOBr and AgBr respectively, suggesting that the transfer of electron from BiOBr to AgBr for AgBr/BiOBr in the dark. The two peaks of Br 3d of 0.33AB move to lower energy compared with pure BiOBr and do not move to high energy in contrast with pure AgBr under illumination because BiOBr occupies the main component in AgBr/BiOBr heterojunction.

Fig. 6 presents the O-K edge of soft X-ray absorption spectra (XAS) for pure BiOBr and 0.33AB respectively. The peak at 527–532 eV is split into t_{2g} and e_g orbital states, which could be attributed to the transition of low energy of 530 eV from O 1s state to the hybridized O2p-Bi5d state. The peak at 535 eV corresponds to hybridization of the O 2p state with the Bi (6s,6p) states [53]. The intensity of peak at 527–532 eV for 0.33AB decreases in contrast with pure BiOBr, which is ascribed to the absence of oxygen atom, i.e., OV. Furthermore, it could be found that the intensity of peak at 533–543 eV for 0.33AB increases compared

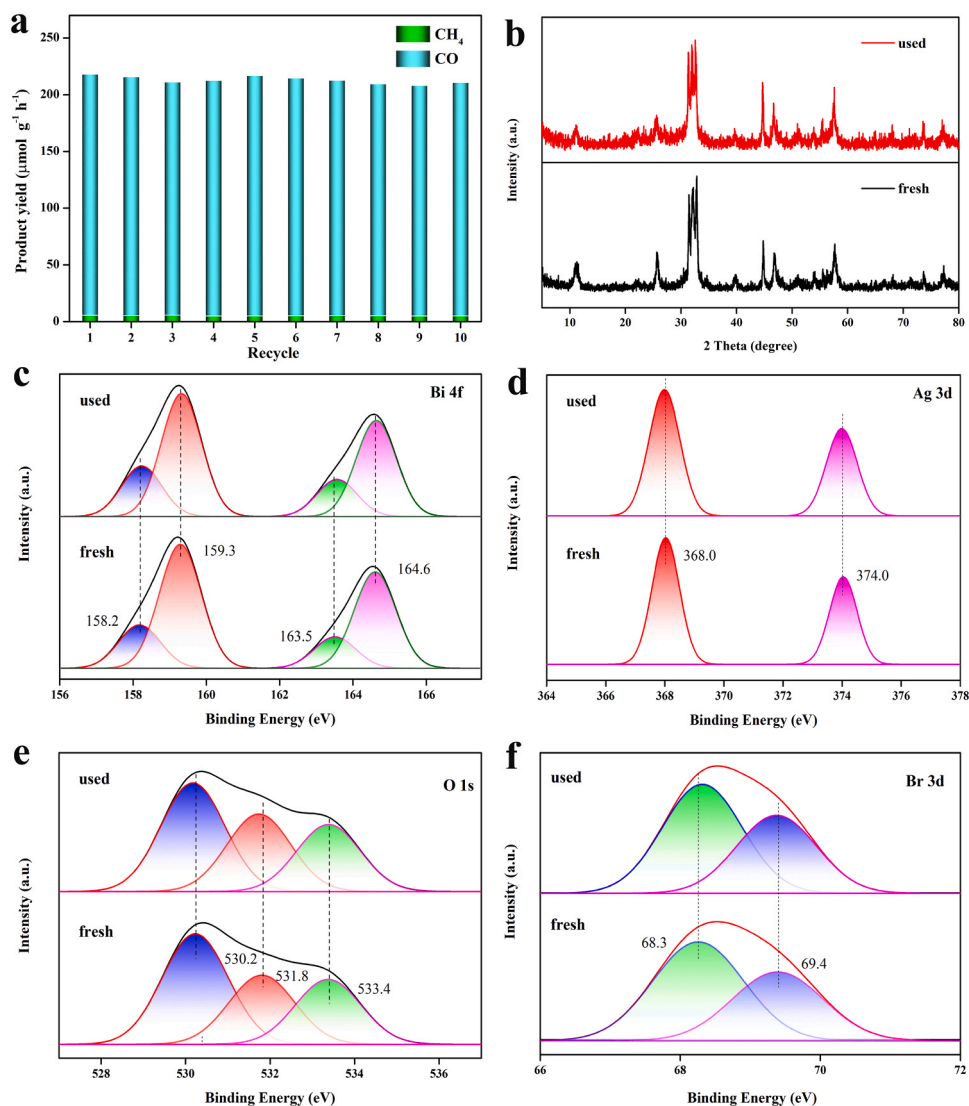


Fig. 7. (a) Recycling photocatalytic performance of 0.33AB. (b) XRD patterns and high-resolution XPS spectra of (c) Bi 4f, (d) Ag 3d, (e) O 1s and (f) Br 3d for the fresh and used catalyst of 0.33AB.

with pure BiOBr , which could be ascribed to the broken local electrostatic balance [54]. In the synthesis process of AgBr/BiOBr heterojunction, the presence of AgBr is apt to induce OV for BiOBr due to the weak $\text{Bi}-\text{O}$ bond. The escaped electrons are liable to be trapped by neighbouring Bi^{3+} ions, which could become to a lower and non-integer valence state ion, such as $\text{Bi}^{(3-x)+}$ ions, inducing the local electrostatic

balance is broken. Therefore, the change of the $\text{O}2\text{p}-\text{O}2\text{p}$ bond strength for AgBr/BiOBr heterojunction compared with pure BiOBr appears to compensate for the charge difference, which could be traced by O K-edge XAS spectra.

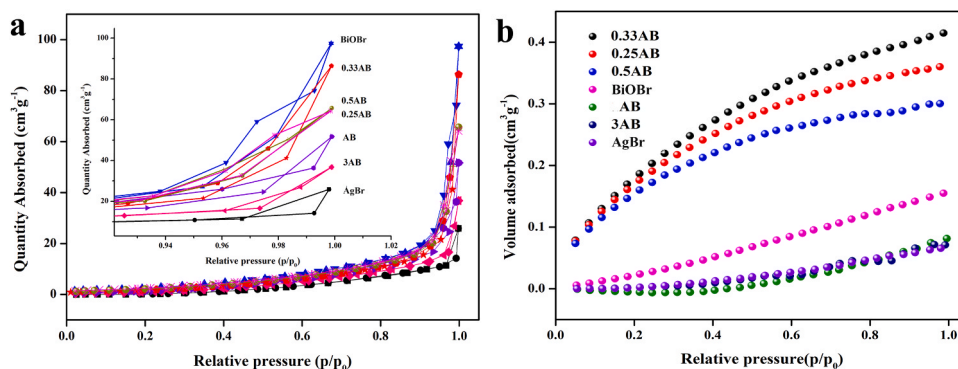


Fig. 8. (a) N_2 physisorption-desorption isotherms and (b) CO_2 adsorption isotherm of samples.

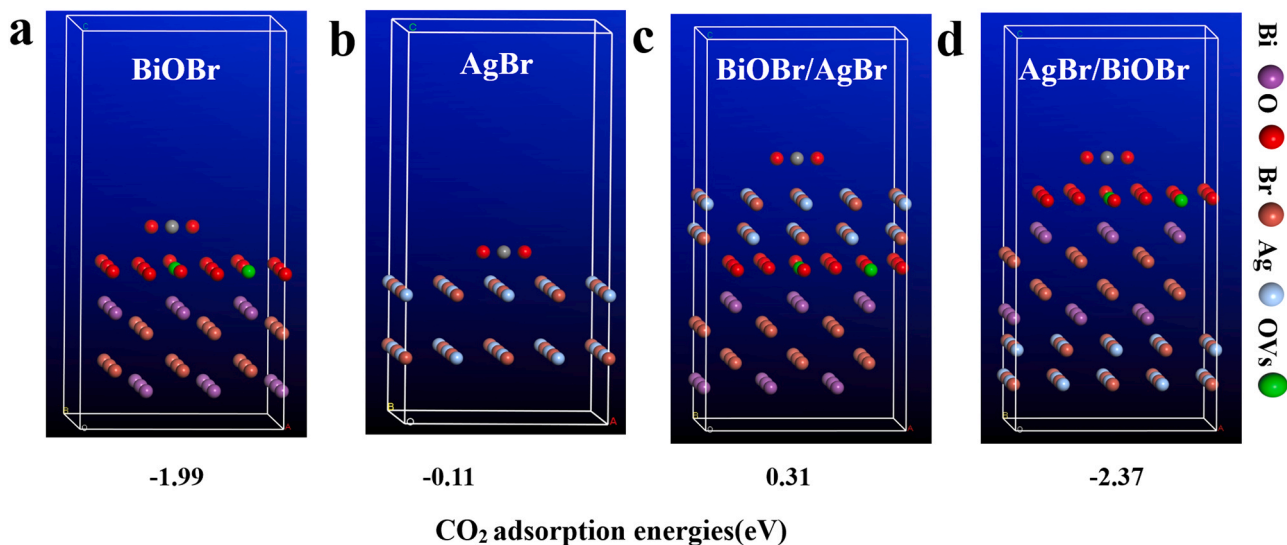


Fig. 9. Optimized geometry structures and CO₂ adsorption energies on (a) AgBr, (b) BiOBr, (c) BiOBr/AgBr and (d) AgBr/BiOBr.

3.5. Stability of catalyst

Fig. 7a presents that 0.33AB maintains a stable yield of CO after five times cycle reaction during 15 h, suggesting that the catalyst has high recyclability and stability. The XRD pattern of fresh 0.33AB is almost the same as the used 0.33AB for five cycles of photocatalytic reaction (Fig. 7b) [55,56]. Furthermore, the stability of used 0.33AB was also detected by survey XPS spectra (Fig. S5) and high-resolution spectra (Fig. 7c, d, e, f), indicating that the XPS spectra of used catalyst are similar with the fresh catalyst. It is found that the difference of XPS peak area ratio (OVs/Bi-O) for 0.33AB before and after the reaction is negligible (Table S4), indicate the improved stability of AgBr/BiOBr heterojunction compared with single AgBr and BiOBr. The SEM and TEM images for used 0.33AB are almost similar to the fresh one (Fig. S6), suggesting that the catalyst is relatively stable.

3.6. Specific surface areas and CO₂ adsorption

Fig. 8a displays the nitrogen (N₂) physisorption desorption isotherm of pure BiOBr, pure AgBr and AgBr/BiOBr with a type IV hysteresis loop, showing the exist of mesoporous structures [57]. The details of N₂ adsorption-desorption and CO₂ adsorption test procedures are illustrated in supporting information. The pore structure of AgBr/BiOBr heterojunction could provide more surface sites for photocatalytic process [58]. The BET surface of pure BiOBr is remarkably larger than those of the other samples. However, 0.33AB exhibits the highest surface area and the largest pore size among all of the heterojunctions (Table S5). Fig. 8b gives CO₂ adsorption isotherm of as-prepare samples. The CO₂ adsorption capacities of pure BiOBr and AgBr are 0.15 and 0.05 m³ g⁻¹, respectively. 0.33AB exhibits the maximum CO₂ adsorption capacity with 0.42 m³ g⁻¹ among the heterojunctions, which is 2.8 and 8.4 times than those of pure BiOBr and AgBr, respectively.

The CO₂ adsorption energies on the surface of pure BiOBr, pure AgBr,

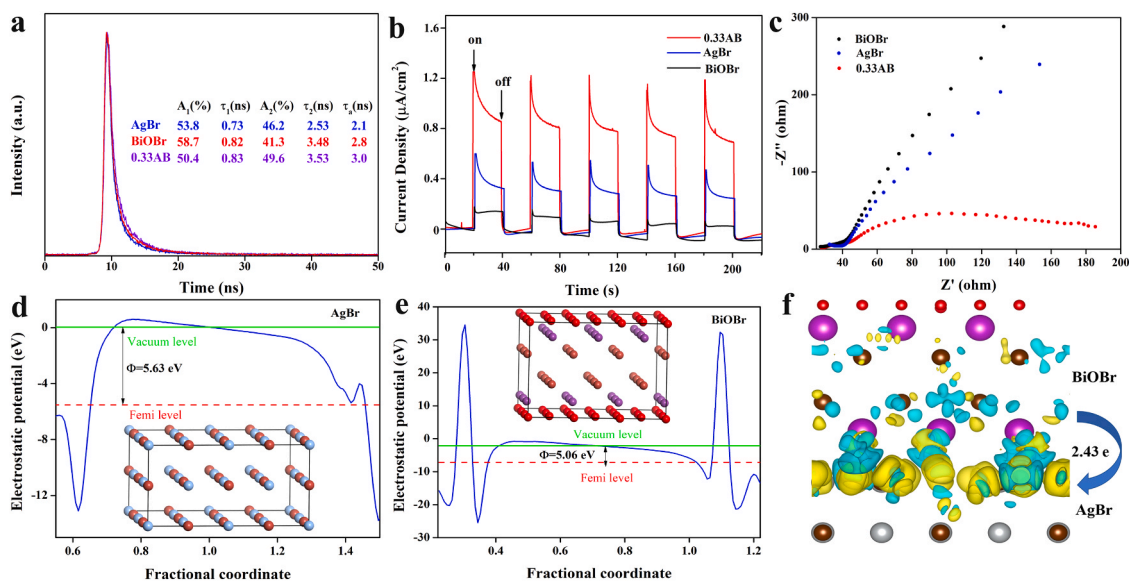


Fig. 10. (a) Time-resolved PL decay (TRPL) curve of as-synthesized samples. (b) Transient photocurrent densities and (c) electrochemical impedance spectroscopy of pure BiOBr, AgBr and 0.33AB. Work functions of (d) pure BiOBr and (e) AgBr. (f) Charge difference distribution of AgBr/BiOBr interfacial structure (the charge accumulation region is in yellow and the charge depletion region is in blue). (For interpretation of the references to colour in this figure legend, the reader is referred to the web version of this article.)

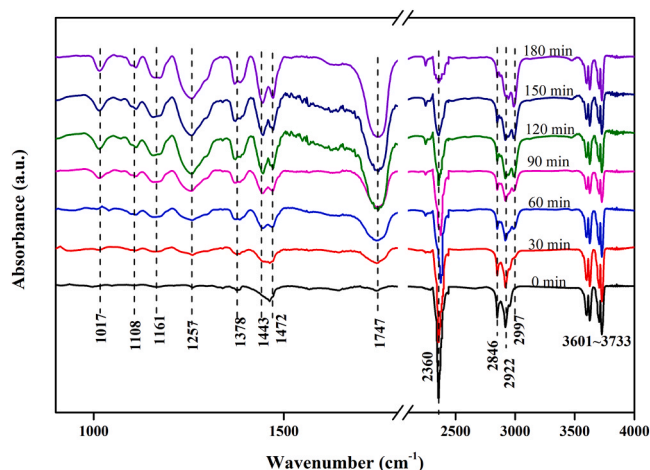


Fig. 11. In situ FTIR spectra on 0.33AB of photocatalytic reduction of CO₂ at different time.

and AgBr or BiOBr sides of AgBr/BiOBr were calculated by DFT method (Fig. 9a-d) [57]. The CO₂ adsorption energies are -1.99 , -0.11 , 0.31 , -2.37 eV for pure BiOBr, pure AgBr, AgBr or BiOBr sides of AgBr/BiOBr, respectively. Negative value of CO₂ adsorption energy means that CO₂ can be adsorbed on the surface of catalysts with exothermal process. More negative value of CO₂ adsorption energy for the catalyst indicates the adsorption is easier and the catalyst is more stable with CO₂ adsorption. Pure BiOBr displays a better CO₂ affinity than pure AgBr. Further, the adsorption energies of CO₂ on the surface of BiOBr side and AgBr side for AgBr/BiOBr are -2.37 eV and 0.31 eV respectively, indicating that CO₂ adsorption prefers on BiOBr side of AgBr/BiOBr rather than AgBr side. Therefore, the theoretical calculations demonstrate that AgBr/BiOBr heterojunctions possess improved CO₂ adsorption capacity, which is consistent with the experimental results.

3.7. Optoelectronic characteristics and charge separation efficiency

Fig. 10a depicts the time-resolved PL decay (TRPL) curve of 0.33AB, pure AgBr and BiOBr. The TRPL curves could be analyzed by the following equation. Where A_1 and A_2 are the corresponding amplitudes, and τ_1 and τ_2 are the fluorescent lifetimes. τ_1 (0.83 ns) and τ_2 (3.53 ns) for 0.33AB were longer than the corresponding values of pure AgBr ($\tau_1 = 0.73$ ns; $\tau_2 = 2.53$ ns) and BiOBr ($\tau_1 = 0.82$ ns; $\tau_2 = 3.48$ ns). Apparently, the average fluorescent lifetimes of pure AgBr (2.1 ns) and BiOBr (2.8 ns) were prolonged to 3.0 ns for 0.33AB according to Eq. (3).

$$\tau_a = \frac{A_1\tau_1^2 + A_2\tau_2^2}{A_1\tau_1 + A_2\tau_2} \quad (3)$$

The extension of the fluorescence lifetime further illustrates that the heterojunction structure can inhibit the combination of photogenerated carriers [58]. Fig. S7 depicted photoluminescence (PL) spectra of pure BiOBr and AgBr/BiOBr heterojunction. The intensity of PL for

AgBr/BiOBr is rapidly quenched at ~ 470 nm compared with pure BiOBr. The quenching degree of the PL intensity for AgBr/BiOBr heterojunction enhances with increasing the amount of AgBr, indicating that the recombination rate of e^-/h^+ pairs for BiOBr is effectively restrained via the incorporation of AgBr [59]. Fig. 10b presents the transient photocurrent tests of pure BiOBr, AgBr and 0.33AB with intermittent light switch on-off, which are considered as an effective method to estimate the separation efficiency of e^-/h^+ pairs. The generated photocurrent of 0.33AB is $1.3 \mu A cm^{-2}$, which is 2.2 and 8.7 times higher than that of pure AgBr and pure BiOBr respectively, indicating that 0.33AB exhibits significantly improved separation efficiency of photoinduced e^-/h^+ pairs [60,61]. Fig. 10c shows the electrochemical impedance plots (EIS) of pure BiOBr, pure AgBr and 0.33AB. The arc radius of 0.33AB is remarkably smaller than that of pure BiOBr and AgBr, implying that 0.33AB has the best interfacial charge transfer efficiency [55]. The work functions of pure BiOBr and AgBr are estimated to be 5.06 eV and 5.63 eV by DFT method [43], respectively (Fig. 10d and e). The work function of pure BiOBr is smaller than that of pure AgBr, suggesting that the electrons of BiOBr could flow into AgBr through the interface for AgBr/BiOBr heterojunction [22]. Fig. 10f presents the charge difference distribution of AgBr/BiOBr heterojunction. The total charges (Δq) value of pure AgBr calculated by the Bader method is -2.43 e, which represents the accumulation of electrons on AgBr, displaying that approximately 2.43 free electrons of BiOBr migrate from to AgBr in AgBr/BiOBr heterojunction due to the different work functions of pure BiOBr and AgBr.

3.8. In situ FTIR and ESR spectra

Fig. 11 shows the in-situ FTIR of 0.33AB in the process of CO₂ photoreduction with pure H₂O at different reaction time. The characteristic vibration band at $1472 cm^{-1}$ is monodentate adsorption of CO₂ (m-CO₂) [62]. The vibration band at $1378 cm^{-1}$ belongs to the bidentate adsorption of CO₂ (b-CO₂) [63]. The absorption band at $1747 cm^{-1}$ is ascribed to the generation of bridging adsorption of CO₂ (c-CO₂) [64]. The vibration band at $1161 cm^{-1}$ is attributed to the formate. The absorption bands at 3601, 3625, 3703 and $3733 cm^{-1}$ are assigned to the characteristic vibration of OH bond in H₂O [$\nu(OH)$], which is consistent with XPS results. The absorption bands at $1256 cm^{-1}$ and $2997 cm^{-1}$ belong to the *COOH group, which is generally considered as the key intermediate for reduction of CO₂ to CO or CH₄ [45]. It is found that the peaks intensities gradually enhanced with extension of the irradiation time. Moreover, the peaks at $1017 cm^{-1}$, $2846 cm^{-1}$ and $2922 cm^{-1}$ are assigned to the characteristic bands of CH₃OH [$\nu(CH_3)$], which is also intermediates of CO₂ photoreduction to CH₄ [65,66]. The asymmetric stretching peak of CO₂ at $2360 cm^{-1}$ is gradually weakened with the extension of the reaction time, indicating that the adsorption of CO₂ on the catalyst surface decreases.

Fig. 12a-c show the in situ ESR spectra of pure AgBr, BiOBr and 0.33AB in air/CO₂ with or without the illumination of light. There is no characteristic ESR signal in any condition of pure AgBr (Fig. 12a). The ESR signals for OV of pure BiOBr and 0.33AB are observed in the air,

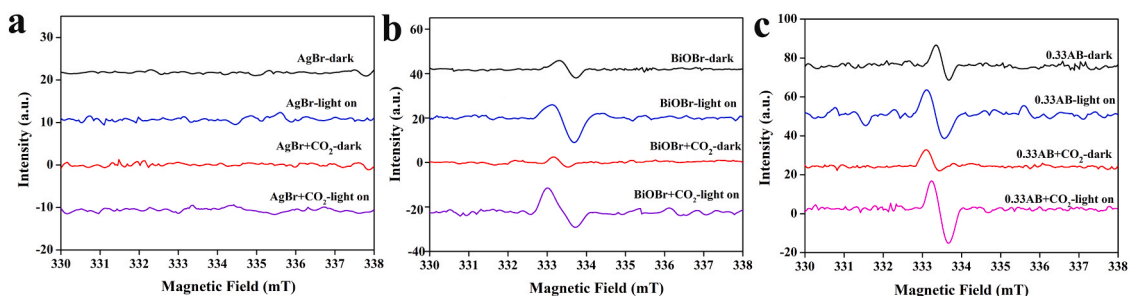


Fig. 12. (a-c). In situ ESR spectra of pure AgBr, pure BiOBr and 0.33AB in different environments.

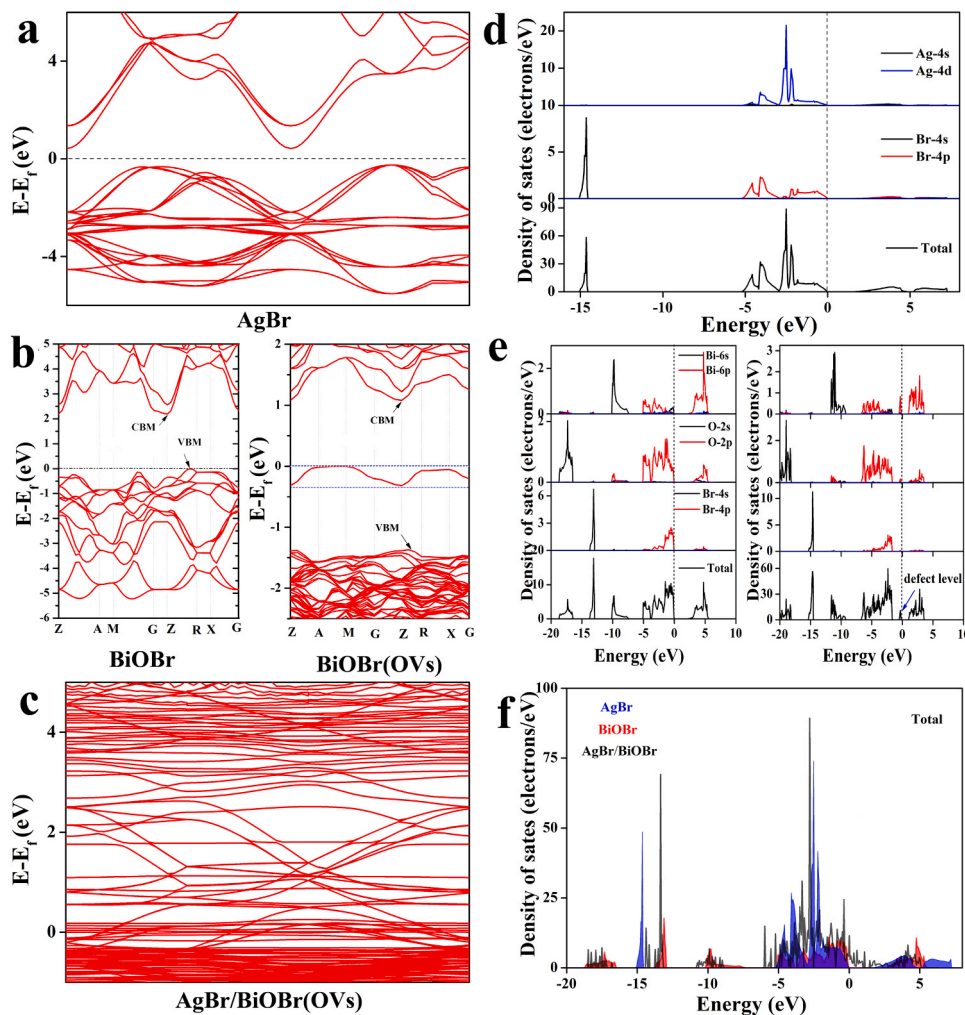


Fig. 13. Calculated band structure of (a) pure AgBr, (b) pure BiOBr (left) and BiOBr (OVs) (right), and (c) AgBr/BiOBr. Calculated DOS of (d) pure AgBr, (e) pure BiOBr (left) and BiOBr (OVs) (right), and (f) AgBr/BiOBr.

illustrating that the peaks increase under the illumination conditions (Fig. 12b and c). The ESR signals of OV are weakened of pure BiOBr and 0.33AB in CO₂ atmosphere, suggesting that CO₂ is absorbed on the surface of pure BiOBr and 0.33AB respectively [67]. The OV signals of pure BiOBr and 0.33AB in CO₂ atmosphere are enhanced under the light irradiation, indicating that the concentration of OV is enhanced after illumination. It is noteworthy that the characteristic ESR signal of 0.33AB is stronger than that of pure BiOBr in air/CO₂ atmosphere, indicating that AgBr/BiOBr heterojunction exhibits the enhanced concentration of OV compared with pure BiOBr.

3.9. Band structure and density of states by DFT calculation

Fig. 13(a-c) display band structure of pure AgBr, pure BiOBr and AgBr/BiOBr (OVs) through DFT calculation. As shown in Fig. 13a, the electron band structure of AgBr is sparse. The conduction band minimum (CBM) of BiOBr is located at Z point, while the valence band maximum (VBM) is located between Z-R (left, Fig. 13b). CBM and VBM of semiconductor are located at different high symmetry points, showing that BiOBr is an indirect band gap semiconductor. The electrons on VBM not only need to absorb energy, but also need to change momentum to transition to the position of CBM for indirect band gap semiconductors [68,69]. This indirect transition can effectively inhibit the recombination of photogenerated carriers, which is conducive to the photocatalytic performance. In particular, a new impurity band appears in BiOBr with OV [62] (right, Fig. 13b). The electron band structure in BiOBr (OVs) is

denser owing to the increased degree of hybridization of atomic orbitals. All of the above results indicate that the introduction of OV in BiOBr facilitates the transport of photogenerated carriers. The VBM of AgBr/BiOBr (OVs) is smoother than that of pure BiOBr, BiOBr (OVs) and AgBr, which indicates that the photogenerated e⁻/h⁺ on AgBr/BiOBr (OVs) has better separation efficiency (Fig. 13c). In addition, the hybridization degree of atomic orbitals in AgBr/BiOBr (OVs) is significantly improved compared with pure BiOBr and AgBr, which makes the band structure of electrons more intensive and facile the electrons transfer in the photocatalytic process. Fig. 13(d-e) show the density of states (DOS) of pure AgBr, pure BiOBr, BiOBr (OVs), and AgBr/BiOBr (OVs) by DFT calculation. As revealed by the calculated DOS of pure AgBr, the VBM is mainly dictated by the Ag 5d and Br 4p orbital, and the CBM consists of the Ag 4s states in pure AgBr (Fig. 13d). The VBM is composed of O 2p and Br 4p orbitals, and the CBM is occupied by Bi 6p orbitals of pure BiOBr (left, Fig. 13e) [70]. The density of states calculation of BiOBr (OVs) further exhibits the existence of impurity levels (right, Fig. 13e). The calculated band gaps of pure AgBr and BiOBr are 2.55 and 2.13 eV, respectively, which are smaller than the experimental value due to the GGA exchange correlation energy function in DFT [40]. The appearance of OV impurity level could reduce the band gap of BiOBr (Fig. S8 and Fig. S9a-b). The existence of OV could increase the photocatalytic performance of CO₂ reduction on 0.33AB (Fig. S10a-b) [71,72]. The VBM consists of BiOBr orbitals and the CBM is occupied by AgBr orbitals for AgBr/BiOBr (OVs) [34] (Fig. 13f). After forming a heterojunction interface in AgBr/BiOBr (OVs), the vacancies of BiOBr

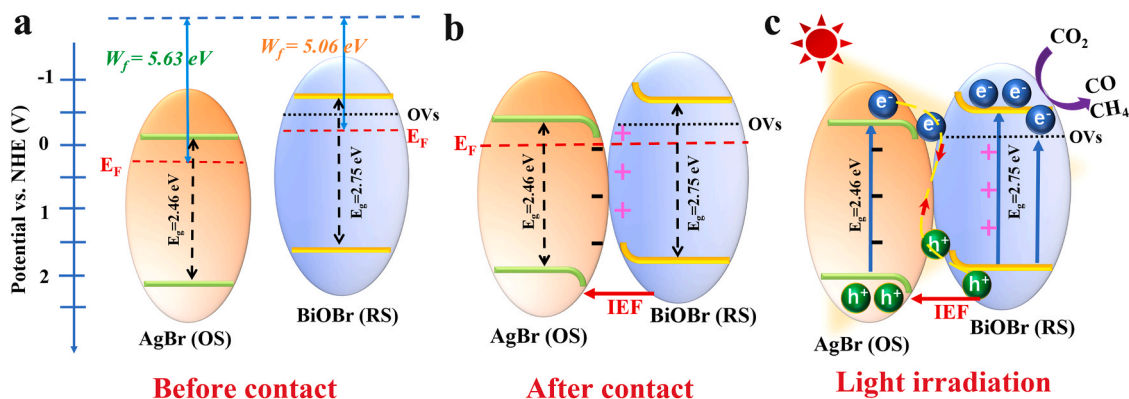


Fig. 14. Band energy positions of AgBr and BiOBr (a) before contact, (b) after contact and (c) under irradiation and S-scheme charge transfer mechanism between AgBr and BiOBr under irradiation.

are filled through the quantum-entangled electronic orbitals, showing the boosting of electron transfer from VB to CB in the AgBr/BiOBr (OVs) [63,73].

3.10. CO₂ photoreduction mechanism

Combined the experimental with DFT calculation, the possible mechanism based on S-scheme heterostructure is proposed (Fig. 14). Before contact, pure BiOBr exhibits a smaller work function and a higher Fermi energy (E_F) than that of pure AgBr (Fig. 14a). When BiOBr intimately contacts with AgBr, the electrons of BiOBr voluntarily flow to the AgBr until their E_F reaches the identical level. The interface area on BiOBr side is positively charged owing to losing electrons, resulting in the formation of electrons depletion region and the upward being of BiOBr band edge. Instead, the interface area near AgBr is negatively charged, which leads to the formation of electrons accumulation layer and downward bending of AgBr band edge (Fig. 14b). Consequently, an inside electric field (IEF) has been formed at interface of AgBr/ BiOBr heterojunction, which prevents the continuous flow of electrons from BiOBr to AgBr. Both BiOBr and AgBr are transformed into excited states through exciting electrons from VB to CB under light irradiation. Then, the e^- accumulated in the CB of AgBr tend to recombine with the h^+ in the VB of BiOBr, driven by Coulomb interaction and IEF, as illustrated in Fig. 14c. This S-scheme band structure is conducive to the spatial separation of photogenerated e^-/h^+ pairs and elimination of relatively useless electrons in the CB of AgBr and holes in the VB of BiOBr. Thus, the electrons will accumulate in the CB of BiOBr and then react with CO₂ to product CO and CH₄. The in situ FTIR spectra indicate that the reaction of CO₂ and H₂O to generate the key intermediates of *COOH and CH₃OH under illumination. Then, the intermediates get electrons and hydrogen protons, creating the product of CO and CH₄. Moreover, the enriched OVs of BiOBr is beneficial to the adsorption and activation of CO₂ molecules, which could lower the overall activation energy barrier of CO₂ reduction. Therefore, AgBr/BiOBr has the better activity in the photocatalytic of CO₂ reduction, which may belong to the synergetic effect of the S-scheme band structure and defects of OVs.

Noticeably, it is observed that AgBr/BiOBr heterojunction is conducive to the improvement of the selectivity of CO. It could be found that the products of CO and CH₄ linearly increase with enhancing the light intensity, indicating that the two reactions display the feature of first-order reaction [73]. The photoreduction of CO₂ to CO and CH₄ are two parallel reactions, in which the rate of CO generation is sped up via the S-scheme heterojunction, thus illustrating a rate-determining step with two electrons and two protons. Therefore, AgBr/BiOBr heterojunction exhibits high selectivity of reduction to CO rather than CH₄.

4. Conclusion

In summary, AgBr/BiOBr heterojunction with OVs was in situ prepared by a facile chemical method under water bath. The photocatalytic reduction activity of CO₂ was systematically explored. It was found that AgBr/BiOBr heterojunction with OVs exhibited higher yields on CO₂ photoreduction reaction compared with pure BiOBr and AgBr. The evolution rate of CO of 0.33AB heterojunction is 9.2 times higher than that of pure BiOBr. The experimental results as well as DFT calculations demonstrate that AgBr/BiOBr heterojunction exhibits an S-scheme band structure, which could improve the utilization of sunlight, charge-separation efficiency, reserve strong redox ability, and enhance adsorption and activation of CO₂. This work provides new insights for in situ synthesis of high efficiency S-scheme heterojunction photocatalyst with defective for CO₂ photoreduction.

CRedit authorship contribution statement

Zerui Miao designed the experiments and wrote the manuscript. Zerui Miao and Qingli Wang synthesized and characterized the samples. Yanfeng Zhang wrote the manuscript. Lingpeng Meng performed DFT calculations. Xuxu Wang conceived the idea of the reaction mechanism. All authors discussed the results.

Declaration of Competing Interest

The authors declare that they have no known competing financial interests or personal relationships that could have appeared to influence the work reported in this paper.

Acknowledgments

This work was supported by the National Natural Science Foundation of China (21973025, 21673043, 21801059), Natural Science Foundation of Hebei of China (B2019205061, B2020205013), Science and Technology Project of Hebei Normal University of China (L2021K01). Postgraduate Innovation Foundation of Hebei Normal University of China (CXZZSS20211055).

Appendix A. Supporting information

Supplementary data associated with this article can be found in the online version at doi:10.1016/j.apcatb.2021.120802.

References

- [1] S. Patial, R. Kumar, P. Raizada, P. Singh, Q. Van Le, E. Lichtfouse, D. Le Tri Nguyen, V.-H. Nguyen, Boosting light-driven CO₂ reduction into solar fuels:

- mainstream avenues for engineering ZnO-based photocatalysts, *Environ. Res.* 197 (2021), 111134, <https://doi.org/10.1016/j.envres.2021.111134>.
- [2] A. Li, T. Wang, C. Li, Z. Huang, Z. Luo, J. Gong, Adjusting the reduction potential of electrons by quantum confinement for selective photoreduction of CO₂ to methanol, *Angew. Chem. Int. Ed.* 58 (2019) 1–6, <https://doi.org/10.1002/ange.201812773>.
 - [3] J. Wu, X. Li, W. Shi, P. Ling, Y. Sun, X. Jiao, S. Gao, L. Liang, J. Xu, W. Yan, C. Wang, Y. Xie, Efficient visible-light-driven CO₂ reduction mediated by defect-engineered BiOBr atomic layers, *Angew. Chem.* 130 (2018) 8855–8859, <https://doi.org/10.1002/ange.2018.03514>.
 - [4] F. He, B. Zhu, B. Cheng, J. Yu, W. Ho, W. Macyk, 2D/2D/0D TiO₂/C₃N₄/Ti₃C₂ MXene composite S-scheme photocatalyst with enhanced CO₂ reduction activity, *Appl. Catal. B Environ.* 272 (2020), 119006, <https://doi.org/10.1016/j.apcatb.2020.119006>.
 - [5] J. Wang, T. Xia, L. Wang, X. Zheng, Z. Qi, C. Gao, J. Zhu, Z. Li, H. Xu, Y. Xiong, Enabling visible-light-driven selective CO₂ reduction by doping quantum dots: trapping electrons and suppressing H₂ evolution, *Angew. Chem. Int. Ed.* 57 (2018) 16447–16451, <https://doi.org/10.1002/ange.201810550>.
 - [6] C. Chen, J. Hu, X. Yang, T. Yang, J. Qu, C. Guo, C.M. Li, Ambient-stable black phosphorus-based 2D/2D S-scheme heterojunction for efficient photocatalytic CO₂ reduction to syngas, *ACS Appl. Mater. Interfaces* 13 (2021) 20162–20173, <https://doi.org/10.1021/acsami.1c03482>.
 - [7] X. Ren, M. Gao, Y. Zhang, Z. Zhang, X. Cao, B. Wang, X. Wang, Photocatalytic reduction of CO₂ on BiOX : effect of halogen element type and surface oxygen vacancy mediated mechanism, *Appl. Catal. B Environ.* 274 (2020), 119063, <https://doi.org/10.1016/j.apcatb.2020.119063>.
 - [8] D. Li, S. Hussain, Y. Wang, C. Huang, P. Li, M. Wang, T. He, ZnSe/CdSe Z-scheme composites with Se vacancy for efficient photocatalytic CO₂ reduction, *Appl. Catal. B Environ.* 286 (2021), 119887, <https://doi.org/10.1016/j.apcatb.2021.119887>.
 - [9] X. Zhang, D. Kim, J. Yan, L.Y.S. Lee, Photocatalytic CO₂ reduction enabled by interfacial S-scheme heterojunction between ultrasmall copper phosphosulfide and g-C₃N₄, *ACS Appl. Mater. Interfaces* 13 (2021) 9762–9770, <https://doi.org/10.1021/acsami.0c17926>.
 - [10] X. Li, Local surface plasma resonance effect enhanced Z-scheme ZnO/Au/g-C₃N₄ film photocatalyst for reduction of CO₂ to CO, *Appl. Catal. B Environ.* 283 (2021), 119638, <https://doi.org/10.1016/j.apcatb.2020.119638>.
 - [11] J. Zhao, Z. Miao, Y. Zhang, G. Wen, L. Liu, X. Wang, X. Cao, B. Wang, Oxygen vacancy-rich hierarchical BiOBr hollow microspheres with dramatic CO₂ photoreduction activity, *J. Colloid Interface Sci.* 593 (2021) 231–243, <https://doi.org/10.1016/j.jcis.2021.02.117>.
 - [12] Q. Chen, H. Long, M. Chen, Y. Rao, X. Li, Y. Huang, In situ construction of biocompatible Z-scheme α-Bi₂O₃/CuBi₂O₄ heterojunction for NO removal under visible light, *Appl. Catal. B Environ.* 272 (2020), 119008, <https://doi.org/10.1016/j.apcatb.2020.119008>.
 - [13] C. Cheng, B. He, J. Fan, B. Cheng, S. Cao, J. Yu, An inorganic/organic S-scheme heterojunction H₂-production photocatalyst and its charge transfer mechanism, *Adv. Mater.* 33 (2021), 2100317, <https://doi.org/10.1002/adma.202100317>.
 - [14] H. Ge, Y. Kuwahara, K. Kusu, H. Yamashita, Plasmon-induced catalytic CO₂ hydrogenation by a nano-sheet Pt/H₂MoO₃-y hybrid with abundant surface oxygen vacancies, *J. Mater. Chem. A* (2021), <https://doi.org/10.1039/D1TA02277F>.
 - [15] C.B. Hiragond, J. Lee, H. Kim, J.-W. Jung, C.-H. Cho, S.-I. In, A novel N-doped graphene oxide enfolded reduced titania for highly stable and selective gas-phase photocatalytic CO₂ reduction into CH₄: an in-depth study on the interfacial charge transfer mechanism, *Chem. Eng. J.* 416 (2021), 127978, <https://doi.org/10.1016/j.cej.2020.127978>.
 - [16] J. Xiong, X. Li, J. Huang, X. Gao, Z. Chen, J. Liu, H. Li, B. Kang, W. Yao, Y. Zhu, CN/rgO@BPQDs high-low junctions with stretching spatial charge separation ability for photocatalytic degradation and H₂O₂ production, *Appl. Catal. B Environ.* 266 (2020), 118602, <https://doi.org/10.1016/j.apcatb.2020.118602>.
 - [17] X. Li, J. Xiong, X. Gao, J. Ma, Z. Chen, B. Kang, J. Liu, H. Li, Z. Feng, J. Huang, Novel BP/BiOBr S-scheme nano-heterojunction for enhanced visible-light photocatalytic tetracycline removal and oxygen evolution activity, *J. Hazard. Mater.* 387 (2020), 121690, <https://doi.org/10.1016/j.jhazmat.2019.121690>.
 - [18] S. Jiang, J. Cao, M. Guo, D. Cao, X. Jia, H. Lin, S. Chen, Novel S-scheme WO₃/RP composite with outstanding overall water splitting activity for H₂ and O₂ evolution under visible light, *Appl. Surf. Sci.* 558 (2021), 149882, <https://doi.org/10.1016/j.apsusc.2021.1482>.
 - [19] X. Li, B. Kang, F. Dong, Z. Zhang, X. Luo, L. Han, J. Huang, Z. Feng, Z. Chen, J. Xu, B. Peng, Z.L. Wang, Enhanced photocatalytic degradation and H₂/H₂O₂ production performance of S-pCN/WO_{2.72} S-scheme heterojunction with appropriate surface oxygen vacancies, *Nano Energy* 81 (2021), 105671, <https://doi.org/10.1016/j.nanoen.2020.105671>.
 - [20] S. Wu, Construction of BiOCl/CuBi₂O₄ S-scheme heterojunction with oxygen vacancy for enhanced photocatalytic diclofenac degradation and nitric oxide removal, *Chem. Eng. J.* 411 (2021), 128555, <https://doi.org/10.1016/j.cej.2021.128555>.
 - [21] Y. Xiao, Z. Ji, C. Zou, Y. Xu, R. Wang, J. Wu, G. Liu, P. He, Q. Wang, T. Jia, Construction of CeO₂/BiOI S-scheme heterojunction for photocatalytic removal of elemental mercury, *Appl. Surf. Sci.* 556 (2021), 149767, <https://doi.org/10.1016/j.apsusc.2021.149767>.
 - [22] P. Xia, S. Cao, B. Zhu, M. Liu, M. Shi, J. Yu, Y. Zhang, Designing a 0D/2D S-scheme heterojunction over polymeric carbon nitride for visible-light photocatalytic inactivation of bacteria, *Angew. Chem. Int. Ed.* 59 (2020) 5218–5225, <https://doi.org/10.1002/anie.201916012>.
 - [23] J. Fu, Q. Xu, J. Low, C. Jiang, J. Yu, Ultrathin 2D/2D WO₃/g-C₃N₄ step-scheme H₂-production photocatalyst, *Appl. Catal. B Environ.* 243 (2019) 556–565, <https://doi.org/10.1016/j.apcatb.2018.11.011>.
 - [24] B. Zhang, M. Zhang, L. Zhang, P.A. Bingham, W. Li, S. Kubuki, PVP surfactant-modified flower-like BiOBr with tunable bandgap structure for efficient photocatalytic decontamination of pollutants, *Appl. Surf. Sci.* 530 (2020), 147233, <https://doi.org/10.1016/j.apsusc.2020.147233>.
 - [25] L. Li, C. Guo, J. Ning, Y. Zhong, D. Chen, Y. Hu, Oxygen-vacancy-assisted construction of FeOOH/CdS heterostructure as an efficient bifunctional photocatalyst for CO₂ conversion and water oxidation, *Appl. Catal. B Environ.* 293 (2021), 120203, <https://doi.org/10.1016/j.apcatb.2021.120203>.
 - [26] H. Li, J. Shang, H. Zhu, Z. Yang, Z. Ai, L. Zhang, Oxygen vacancy structure associated photocatalytic water oxidation of BiOCl, *ACS Catal.* 6 (2016) 8276–8285, <https://doi.org/10.1021/acscatal.6b02613>.
 - [27] M. Guan, C. Xiao, J. Zhang, S. Fan, R. An, Q. Cheng, J. Xie, M. Zhou, B. Ye, Y. Xie, Vacancy associates promoting solar-driven photocatalytic activity of ultrathin bismuth oxychloride nanosheets, *J. Am. Chem. Soc.* 135 (2013) 10411–10417, <https://doi.org/10.1021/ja402956f>.
 - [28] J. Ma, An efficient and robust exfoliated bentonite/Ag₃PO₄/AgBr plasmonic photocatalyst for degradation of parabens, *RSC Adv.* 10 (2020) 16027, <https://doi.org/10.1039/d0ra02455d>.
 - [29] C. Hu, T.-R. Su, T.-J. Lin, C.-W. Chang, K.-L. Tung, Yellowish and blue luminescent graphene oxide quantum dots prepared via a microwave-assisted hydrothermal route using H₂O₂ and KMnO₄ as oxidizing agents, *New J. Chem.* 42 (2018) 3999–4007, <https://doi.org/10.1039/C7NJ03337K>.
 - [30] L. Ye, J. Liu, C. Gong, L. Tian, T. Peng, L. Zan, Two different roles of metallic Ag on Ag/AgX/BiOX (X = Cl, Br) visible light photocatalysts: surface plasmon resonance and S-scheme bridge, *ACS Catal.* 2 (2012) 1677–1683, <https://doi.org/10.1021/cs300213m>.
 - [31] S. Yao, S. Xue, J. Zhang, X. Shen, Characterization and mechanism analysis of AgBr mixed cuboid WO₃ rods with enhanced photocatalytic activity, *RSC Adv.* 6 (2016) 93436–93444, <https://doi.org/10.1039/C6RA16442K>.
 - [32] P. Murugesan, S. Narayanan, M. Manickam, Experimental studies on photocatalytic reduction of CO₂ using AgBr decorated g-C₃N₄ composite in TEA mediated system, *J. CO₂ Util.* 22 (2017) 250–261, <https://doi.org/10.1016/j.jcou.2017.10.012>.
 - [33] M.F. Ehsan, T. He, In situ synthesis of ZnO/ZnTe common cation heterostructure and its visible-light photocatalytic reduction of CO₂ into CH₄, *Appl. Catal. B Environ.* 166–167 (2015) 345–352, <https://doi.org/10.1016/j.apcatb.2014.11.058>.
 - [34] X.-D. Wang, Y.-H. Huang, J.-F. Liao, Y. Jiang, L. Zhou, X.-Y. Zhang, H.-Y. Chen, D.-B. Kuang, In situ construction of a Cs₂SnI₆ perovskite nanocrystal/SnS₂ nanosheet heterojunction with boosted interfacial charge transfer, *J. Am. Chem. Soc.* 141 (2019) 13434–13441, <https://doi.org/10.1021/jacs.9b04482>.
 - [35] M. Zhang, Q. Ying, Z. Zhang, AgBr/BiOBr nano-heterostructure-decorated polyacrylonitrile nanofibers: a recyclable high-performance photocatalyst for dye degradation under visible-light irradiation, *Polymers* 11 (2019) 1718, <https://doi.org/10.3390/polym11101718>.
 - [36] T. Feng, J. Liang, Z. Ma, M. Li, M. Tong, Bactericidal activity and mechanisms of BiOBr-AgBr under both dark and visible light irradiation conditions, *Colloids Surf. B Biointerfaces* 167 (2018) 275–283, <https://doi.org/10.1016/j.colsurfb.2018.04.022>.
 - [37] H. Cheng, B. Huang, P. Wang, Z. Wang, Z. Lou, J. Wang, X. Qin, X. Zhang, Y. Dai, In situ ion exchange synthesis of the novel Ag/AgBr/BiOBr hybrid with highly efficient decontamination of pollutants, *Chem. Commun.* 47 (2011) 7054, <https://doi.org/10.1039/c1cc11525a>.
 - [38] G. Kresse, J. Furthmüller, Efficient iterative schemes for ab initio total-energy calculations using a plane-wave basis set, *Phys. Rev. B* 54 (1996) 11169–11186, <https://doi.org/10.1103/PhysRevB.54.11169>.
 - [39] J.P. Perdew, K. Burke, M. Ernzerhof, Generalized gradient approximation made simple, *Phys. Rev. Lett.* 77 (1996) 3865–3868, <https://doi.org/10.1103/PhysRevLett.77.3865>.
 - [40] J.P. Perdew, J.A. Chevary, S.H. Vosko, K.A. Jackson, M.R. Pederson, D.J. Singh, C. Fiolhais, Atoms, molecules, solids, and surfaces: applications of the generalized gradient approximation for exchange and correlation, *Phys. Rev. B* 46 (1992) 6671–6687, <https://doi.org/10.1103/PhysRevB.46.6671>.
 - [41] X. Wu, Y.H. Ng, L. Wang, Y. Du, S.X. Dou, R. Amal, J. Scott, Improving the photo-oxidative capability of BiOBr via crystal facet engineering, *J. Mater. Chem. A* 5 (2017) 8117–8124, <https://doi.org/10.1039/C6TA10964K>.
 - [42] X. Tian, Y. Sun, J. He, X. Wang, J. Zhao, S. Qiao, F. Li, Surface P atom grafting of g-C₃N₄ for improved local spatial charge separation and enhanced photocatalytic H₂ production, *J. Mater. Chem. A* 7 (2019) 7628–7635, <https://doi.org/10.1039/C9TA00129H>.
 - [43] P. Wang, Y. Liu, N. Jiang, R. Jing, S. Li, Q. Zhang, H. Liu, J. Xiu, Z. Li, Y. Liu, Double S-scheme AgBr heterojunction co-modified with g-C₃N₄ and black phosphorus nanosheets greatly improves the photocatalytic activity and stability, *J. Mol. Liq.* 329 (2021), 115540, <https://doi.org/10.1016/j.molliq.2021.115540>.
 - [44] J. Guo, Y. Liu, Y. Hao, Y. Li, X. Wang, R. Liu, F. Li, Comparison of importance between separation efficiency and valence band position: the case of heterostructured Bi₂O₃/α-Bi₂O₃ photocatalysts, *Appl. Catal. B Environ.* 224 (2018) 841–853, <https://doi.org/10.1016/j.apcatb.2017.11.046>.
 - [45] T. Jia, J. Wu, J. Song, Q. Liu, J. Wang, Y. Qi, P. He, X. Qi, L. Yang, P. Zhao, In situ self-growing 3D hierarchical BiOBr/BiOI₂ Z-scheme heterojunction with rich oxygen vacancies and iodine ions as carriers transfer dual-channels for enhanced photocatalytic activity, *Chem. Eng. J.* 396 (2020), 125258, <https://doi.org/10.1016/j.cej.2020.125258>.

- [46] J. Fu, K. Jiang, X. Qiu, J. Yu, M. Liu, Product selectivity of photocatalytic CO₂ reduction reactions, *Mater. Today* 32 (2020) 222–243, <https://doi.org/10.1016/j.mattod.2019.06.009>.
- [47] X. Li, Y. Sun, J. Xu, Y. Shao, J. Wu, X. Xu, Y. Pan, H. Ju, J. Zhu, Y. Xie, Selective visible-light-driven photocatalytic CO₂ reduction to CH₄ mediated by atomically thin CuIn₅S₈ layers, *Nat. Energy* 4 (2019) 690–699, <https://doi.org/10.1038/s41560-019-0431-1>.
- [48] Q. Huang, S. Tian, D. Zeng, X. Wang, W. Song, Y. Li, W. Xiao, C. Xie, Enhanced photocatalytic activity of chemically bonded TiO₂/graphene composites based on the effective interfacial charge transfer through the C–Ti bond, *ACS Catal.* 3 (2013) 1477–1485, <https://doi.org/10.1021/cs400080w>.
- [49] L. Liu, C. Zhao, Y. Li, Spontaneous dissociation of CO₂ to CO on defective surface of Cu(I)/TiO_{2-x} nanoparticles at room temperature, *J. Phys. Chem. C* 116 (2012) 7904–7912, <https://doi.org/10.1021/jp300932b>.
- [50] H. Wang, D. Yong, S. Chen, S. Jiang, X. Zhang, W. Shao, Q. Zhang, W. Yan, B. Pan, Y. Xie, Oxygen-vacancy-mediated exciton dissociation in BiOBr for boosting charge-carrier-involved molecular oxygen activation, *J. Am. Chem. Soc.* 140 (2018) 1760–1766, <https://doi.org/10.1021/jacs.7b10997>.
- [51] X. Liu, C. Bie, B. He, B. Zhu, L. Zhang, B. Cheng, OD/2D NiS/CdS nanocomposite heterojunction photocatalyst with enhanced photocatalytic H₂ evolution activity, *Appl. Surf. Sci.* 554 (2021), 149622, <https://doi.org/10.1016/j.apsusc.2021.149622>.
- [52] Z. Geng, X. Kong, W. Chen, H. Su, Y. Liu, F. Cai, G. Wang, J. Zeng, Oxygen vacancies in ZnO nanosheets enhance CO₂ electrochemical reduction to CO, *Angew. Chem.* 130 (2018) 6162–6167, <https://doi.org/10.1002/ange.201711255>.
- [53] P. Sharma, A. Yogi, A. Kumar, R. Li, G. Sharma, J. Fan, V. Sathe, Q. Li, W. Ren, S. Cao, Spin-lattice correlation in Eu³⁺ doped antiferromagnet TmFeO₃, *Phys. Chem. Chem. Phys.* 21 (2019) 19181–19191, <https://doi.org/10.1039/C9CP02770J>.
- [54] F. Frati, M.O.J.Y. Hunault, F.M.F. de Groot, Oxygen K-edge X-ray absorption spectra, *Chem. Rev.* 120 (2020) 4056–4110, <https://doi.org/10.1021/acs.chemrev.9b00439>.
- [55] T. Liu, K. Yang, H. Gong, Z. Jin, Visible-light driven S-scheme Mn_{0.2}Cd_{0.8}S/CoTiO₃ heterojunction for photocatalytic hydrogen evolution, *Renew. Energy* 173 (2021) 389–400, <https://doi.org/10.1016/j.renene.2021.03.146>.
- [56] J. Xiong, X. Li, J. Huang, X. Gao, Z. Chen, J. Liu, H. Li, B. Kang, W. Yao, Y. Zhu, CN/rGO@BPQDs high-low junctions with stretching spatial charge separation ability for photocatalytic degradation and H₂O₂ production, *Appl. Catal. B Environ.* 266 (2020), 118602, <https://doi.org/10.1016/j.apcatb.2020.118602>.
- [57] X. Xu, J. Wang, Y. Shen, An interface optimization strategy for g-C₃N₄-based S-scheme heterojunction photocatalysts, *Langmuir* 37 (2021) 7254–7263, <https://doi.org/10.1021/acs.langmuir.1c01009>.
- [58] Y. Jia, W. Zhang, J. Yeon Do, M. Kang, C. Liu, Z-scheme SnFe₂O₄/α-Fe₂O₃ microoctahedron with intimate interface for photocatalytic CO₂ reduction, *Chem. Eng. J.* 402 (2020), 126193, <https://doi.org/10.1016/j.cej.2020.126193>.
- [59] X. Li, W. Wang, F. Dong, Z. Zhang, L. Han, X. Luo, J. Huang, Z. Feng, Z. Chen, G. Jia, T. Zhang, Recent advances in noncontact external-field-assisted photocatalysis: from fundamentals to applications, *ACS Catal.* 11 (2021) 4739–4769, <https://doi.org/10.1021/acs.catal.0c05354>.
- [60] W. Bi, Y. Hu, N. Jiang, L. Zhang, H. Jiang, X. Zhao, C. Wang, C. Li, Ultra-fast construction of plaque-like Li₂TiO₃/TiO₂ heterostructure for efficient gas-solid phase CO₂ photoreduction, *Appl. Catal. B Environ.* 269 (2020), 118810, <https://doi.org/10.1016/j.apcatb.2020.118810>.
- [61] S. Xiao, D. Zhang, D. Pan, W. Zhu, P. Liu, Y. Cai, G. Li, H. Li, A chloroplast structured photocatalyst enabled by microwave synthesis, *Nat. Commun.* 10 (2019) 1570, <https://doi.org/10.1038/s41467-019-09509-y>.
- [62] A. Zhou, Y. Dou, C. Zhao, J. Zhou, X.-Q. Wu, J.-R. Li, A leaf-branch TiO₂/carbon@MOF composite for selective CO₂ photoreduction, *Appl. Catal. B Environ.* 264 (2020), 118519, <https://doi.org/10.1016/j.apcatb.2019.118519>.
- [63] S. Gong, G. Zhu, R. Wang, F. Rao, X. Shi, J. Gao, Y. Huang, C. He, M. Hojamberdiev, Synergistically boosting highly selective CO₂-to-CO photoreduction over BiOCl nanosheets via in-situ formation of surface defects and non-precious metal nanoparticles, *Appl. Catal. B Environ.* 297 (2021), 120413, <https://doi.org/10.1016/j.apcatb.2021.120413>.
- [64] M. Zheng, X. Ma, J. Hu, X. Zhang, D. Li, W. Duan, Novel recyclable BiOBr/Fe₃O₄/RGO composites with remarkable visible-light photocatalytic activity, *RSC Adv.* 10 (2020) 19961–19973, <https://doi.org/10.1039/D0RA01668C>.
- [65] Y. Liu, C. Miao, P. Yang, Y. He, J. Feng, D. Li, Synergistic promotional effect of oxygen vacancy-rich ultrathin TiO₂ and photochemical induced highly dispersed Pt for photoreduction of CO₂ with H₂O, *Appl. Catal. B Environ.* 244 (2019) 919–930, <https://doi.org/10.1016/j.apcatb.2018.12.028>.
- [66] Y. Wang, Z. Zhang, L. Zhang, Z. Luo, J. Shen, H. Lin, J. Long, J.C.S. Wu, X. Fu, X. Wang, C. Li, Visible-light driven overall conversion of CO₂ and H₂O to CH₄ and O₂ on 3D-SiC@2D-MoS₂ heterostructure, *J. Am. Chem. Soc.* 140 (2018) 14595–14598, <https://doi.org/10.1021/jacs.8b09344>.
- [67] B. Wang, X. Wang, L. Lu, C. Zhou, Z. Xin, J. Wang, X. Ke, G. Sheng, S. Yan, Z. Zou, Oxygen-vacancy-activated CO₂ splitting over amorphous oxide semiconductor photocatalyst, *ACS Catal.* 8 (2018) 516–525, <https://doi.org/10.1021/acscatal.7b02952>.
- [68] A.M. Ganose, M. Cuff, K.T. Butler, A. Walsh, D.O. Scanlon, Interplay of orbital and relativistic effects in bismuth oxyhalides: BiOF, BiOCl, BiOBr, and BiOI, *Chem. Mater.* 28 (2016) 1980–1984, <https://doi.org/10.1021/acs.chemmater.6b00349>.
- [69] J. Wang, Y. Huang, J. Guo, J. Zhang, X. Wei, F. Ma, Optoelectronic response and interfacial properties of BiOI/BiOX (X = F, Cl, Br) heterostructures based on DFT investigation, *J. Solid State Chem.* 284 (2020), 121181, <https://doi.org/10.1016/j.jssc.2020.121181>.
- [70] H. Li, F. Qin, Z. Yang, X. Cui, J. Wang, L. Zhang, New reaction pathway induced by plasmon for selective benzyl alcohol oxidation on BiOCl possessing oxygen vacancies, *J. Am. Chem. Soc.* 139 (2017) 3513–3521, <https://doi.org/10.1021/jacs.6b12850>.
- [71] H. Li, J. Shi, K. Zhao, L. Zhang, Sustainable molecular oxygen activation with oxygen vacancies on the {001} facets of BiOCl nanosheets under solar light, *Nanoscale* 6 (2014) 14168–14173, <https://doi.org/10.1039/C4NR04810E>.
- [72] Y. Mao, P. Wang, L. Li, Z. Chen, H. Wang, Y. Li, S. Zhan, Unravelling the synergy between oxygen vacancies and oxygen substitution in BiO_{2-x} for efficient molecular-oxygen activation, *Angew. Chem. Int. Ed.* 59 (2020) 3685–3690, <https://doi.org/10.1002/anie.201914001>.
- [73] G. Yin, X. Huang, T. Chen, W. Zhao, Q. Bi, J. Xu, Y. Han, F. Huang, Hydrogenated blue titania for efficient solar to chemical conversions: preparation, characterization, and reaction mechanism of CO₂ reduction, *ACS Catal.* 8 (2018) 1009–1017, <https://doi.org/10.1021/acscatal.7b03473>.